Au/WO3 nanocomposite based photocatalyst for enhanced solar photocatalytic activity

Margaux Desseigne, Véronique Madigou, Marie-Vanessa Coulet, Olivier Heintz, Virginie Chevallier, Madjid Arab

Au/WO_3 nanocomposite based photocatalyst for enhanced solar photocatalytic activity

Margaux Desseigne *[a], **Véronique Madigou** [a], **Marie Vanessa Coulet** [b], **Olivier Heintz** [c], **Virginie Chevallier** [a], **Madjid Arab** *[a]

[a] Université de Toulon, Aix Marseille Univ, CNRS, IM2NP, Toulon, France

[b] Aix-Marseille University, CNRS, MADIREL (UMR 7246), Campus de St Jérôme, 13013, Marseille Cedex, France

[c] Laboratoire Interdisciplinaire Carnot de Bourgogne (UMR 6303 CNRS), Université de Bourgogne Franche-Comté BP 47 870, 21078, Dijon, France

* Corresponding authors – E-mail: dr.desseigne@gmail.com and madjid.arab@univ-tln.fr

Abstract

Gold nanoparticles (AuNPs) were loaded on tungsten trioxide (WO_3) platelet-like support by a simple impregnation deposition technique at room temperature. Textural, structural and electrical properties were characterized for the as prepared material. The SEM/TEM investigations revealed that formed AuNPs possess a mean diameter of 7 nm and a preferential deposition on the (020) planes of the orthorhombic WO_3 structure. The photodegradation efficiency was evaluated under solar light irradiation using dye pollutant solutions such as rhodamine B (RhB), methylene blue (MB) and methyl orange (MO). According to the affinity between the organic pollutant and the catalyst support, the adsorption/photocatalysis yield and the degradation pathway differ. It was observed that MB created strong electrostatic bonds with the catalyst support while RhB and MO did not adsorb on Au/WO_3 hybrid sample. Photocatalytic tests revealed a high performance of Au/WO_3 photocatalyst with a complete degradation in 90 min for a cationic dye mainly due to the oxidation by the hydroxyl reactive oxidant species. LC-MS analyses confirmed a higher decomposition with gold compared to bare WO_3 on the MB pollutant and results permit to propose a degradation pathway.

Keywords

Photocatalyst; Au/WO_3 nanocomposite; Solar photocatalysis; Dyes degradation

1. Introduction

Water pollution is considered as one of the most prominent issue of global public health challenge with more and more serious situation [1–4]. Nearly one third of the population around the world cannot access clean drinking water while the more developed countries have to handle new water treatment issues mainly due to pharmaceutical and agricultural wastes [5–7]. In the past few decades, photocatalytic degradation of pollutants in aqueous solution based on semiconductor-photocatalysts has become an effective approach to address those issues [8–12]. Numerous photocatalysts have been proposed for the decomposition of organic pollutants such as titanium oxide (TiO_2) [13–15] and zinc oxide (ZnO) [16–18], the most studied ones. However, because of their high band gap energy (> 3.2 eV) corresponding to a maximum wavelength of 392 nm, only 4 % of solar light is effective with these photocatalysts. To meet the challenges of sustainability and green chemistry, the photocatalytic field has to develop new materials capable to absorb visible radiation in order to better harness solar light, a free and clean energy. Different strategies are efficient to extend optical absorption to visible light. One of them consists in doping high band gap photocatalysts such as previously cited TiO_2 or ZnO [19–21]; another path is the choice of alternative compounds with a narrower band gap [22–24]. In the present work, tungsten trioxide (WO_3) has been selected as photocatalyst material to study the degradation of different dyes by photocatalytic reaction. WO_3 is a n-type semiconductor with an indirect band gap ranging between 2.4 and 2.8 eV [25] which endows it a higher solar energy utilization efficiency than TiO_2 or ZnO. The photogenerated holes (h^+) in its valence band (VB) have a strong oxidation ability thanks to a VB potential (E_{VB}) reaching 2.7-3.4 eV (vs. normal hydrogen electrode, NHE) [26]. Nevertheless, WO_3 has a low photocatalytic activity because its conduction band potential (E_{CB}) is positive and the recombination of photogenerated electron-hole pairs is greatly facilitated [27]. In order to enhance the photocatalytic efficiency of WO_3, gold nanoparticles (AuNPs) can be deposited on its surface as metal particles to contribute to the photoelectron-hole separation, prolong the

charge carrier lifetime and extend the visible light absorption range to accelerate electron transfer kinetics [28]. Among the different synthesis methods for the deposition of AuNPs on WO_3, one can cite aerosol-assisted chemical vapor deposition [29,30], photochemical deposition [31], cationic adsorption [32], in situ redox reaction [33,34] or ultrasonic method [35]. In this work, we presented a highly efficient photocatalyst based on gold nanoparticles deposition on nanostructured platelet-like tungsten oxide semiconductor. Gold nanoparticles was expected to enhance the photogeneration of charge carrier due to a higher work function than WO_3 and its plasmonic properties. The nanocomposite Au/WO_3 was prepared by a novel and facile method consisting in forming gold nanoparticles onto WO_3 platelets involving a simple impregnation-reduction route at room temperature and without any further treatment. The as-synthesized Au/WO_3 nanocomposite is fully characterized in terms of texture, structure and electrical properties. A deep analysis is performed to understand the influence of AuNPs deposition onto the oxide surface. The photocatalytic performance was evaluated on the degradation of three dyes: rhodamine B, methylene blue and methyl orange. Besides, scavengers tests were investigated in order to study the dye decomposition process by oxidative species. Finally, a specific investigation by liquid chromatography coupled with mass spectroscopy was performed in the case of MB degraded by our photocatalysts. This investigation results in a degradation pathway proposition and highlights the interest to associate gold with WO_3 for solar photocatalytic degradation.

2. Materials and methods

2.1. Chemicals

Sodium tungstate dihydrate ($NaWO_4$, $2H_2O$; CAS Nb. 10213-10-2), gold (III) chloride trihydrate ($HAuCl_4$,$3H_2O$; CAS Nb. 16961-25-4) and sodium borohydride ($NaBH_4$; CAS Nb. 16940-66-2) were purchased from Sigma-Aldrich. Rhodamine B (CAS Nb. 81-88-9), methylene blue (CAS Nb. 61-73-4) and methyl orange (CAS Nb. 547-58-0) were purchased from ChemLab. All reagents were used as received without any further purification. Deionized water with a resistivity of 18 MΩ.cm was used.

2.2. Synthesis of Au/WO_3 composite

The composite material was obtained in two steps. The first one is the synthesis of a nanostructured semiconductor based on WO_3 subsequently use as a support for the second step consisting in the formation of gold nanoparticles onto the oxide particles.

2.2.1. Preparation of WO_3 support

The WO_3 nanoparticles were synthesized in our laboratory following the same method reported in a previous work (Dirany et al., 2016a, 2016b). Firstly, 1 g of the tungsten precursor was dissolved in 20 mL of water and a 2 $mol.L^{-1}$ HCl solution was added to reduce the pH value to 1. Then, the solution was transferred in a warm bath at 70 °C and stirred until complete evaporation of the solvent is achieved. 60 mL of a 2 $mol.L^{-1}$ HCl solution was added to the obtained pale yellow powder and the solution was heated at 40 °C during 24 hours under stirring. Secondly, an aging step was applied to the yellow solution in an oven under air flow at 80 °C during 96 hours. At the end, a bright yellow powder was obtained, washed several time with water/ethanol by centrifugation and dried at 60 °C in an oven. A thermal treatment under air at 500 °C lead to WO_3 nanoparticles with an orthorhombic structure and a platelet shape of 60-70 nm thickness size and 300 nm square basal length.

2.2.2. Preparation of Au/WO_3 nanocomposite

Gold nanoparticles were formed on the surface of nanostructured tungsten oxide using an impregnation-reduction technique at room temperature. First, an amount of previously synthesized WO_3 was dispersed in a 10^{-3} $mol.L^{-1}$ gold precursor solution. The powder concentration was 4 $mg.mL^{-1}$. The mixture was stirred in the darkness during 48 hours before to add 0.15 mmol of freshly prepared $NaBH_4$ solution. The reduction took place and led to the nucleation and growth of gold nanoparticles by the state modification from auric ions to metallic state. After the reductive addition which was executed in an ice-cooled bath, the powder was washed with water/ethanol by centrifugation and dried overnight under air flow at 60 °C in an oven. Considering the ratio between the gold precursor and the WO_3 suspension, the gold loading on the oxide support was assumed to be 5 wt. %. The as-prepared composite was labelled Au/WO_3.

2.3. Characterizations

The samples were observed by scanning electron microscopy (SEM, SUPRA 40Vp GEMINI Zeiss with in-lens detector) and transmission electron microscopy (TEM, JEOL JEM2010 and JEOL JEM3010). Chemical analyses were performed by inductively coupled plasma (ICP, ICP AES iCAP 6500 DUO – Thermo Scientific and ICP AES iCAP 7400 Radial – Thermo Scientific). Powder X-ray diffraction (XRD) was used to define the crystallinity and the crystallographic structure of samples. Diffraction patterns were acquired using an Empyrean Panalytical diffractometer working with Cu K_α radiation in a 2θ range scanning from 20 to 70 degrees (λ = 0.15440 nm, voltage = 45 kV and intensity = 35 mA). The oxidation state of the elements as well as the metal-oxide interaction was monitored using X-ray photoelectron spectroscopy (XPS) measurements. The XPS spectra were acquired with a PHI 5000 Versaprobe apparatus with an Al $K_{\alpha 1}$ radiation source (energy = 1486.7 eV, accelerating voltage = 15 kV, power = 50 W and spot size diameter = 200 µm). Pass energies of 187 eV and 58.7 eV were used for survey spectra and high-resolution windows, respectively. The texture was characterized by gas adsorption. Sorption isotherms were measured at -196 °C using BELSORP Max 1 apparatus. Prior to the measurement, the samples were treated at 150 °C under vacuum for 15 hours in order to remove any adsorbed species. Optical absorbance and UV-visible diffuse reflectance spectra (DRS) were collected with a SHIMADZU 2600 UV-Vis/NIR spectrophotometer. The reflectance (R_∞) was recorded with respect to $BaSO_4$ reference and the band-gap energy was calculated according to the Kubelka-Munk function expressing the relative absorption coefficient by the as-follow equation: $F(R_\infty) = (1 - R_\infty)^2/2R_\infty$. The separation efficiency of the photogenerated charges was determined using photoresistance response (PRR) analysis. Results were collected using a SiO_2/Si wafer covered with Pt electrodes and the measurements were performed with a Keithley 2611 digital multimeter. The LC-ESI-MS analyses were performed on a UHPLC-HRMS system (Dionex Ultimate 3000 Rapid Separation; Thermo Fisher Scientific) coupled with a QToF Impact II mass spectrometer (Bruker Daltonics, Bremen, Germany) in positive and negative ionization modes. The

separations were carried out with an analytical core-shell reversed-phase column (150 × 2.1 mm, 1.7 µm, Kinetex Phenyl-Hexyl; Phenomenex, Le Pecq, France). **See supplementary information for more details.**

2.4. Photocatalytic activity

The photocatalytic performances were evaluated on different model pollutants such as dye molecules. Rhodamine B (RhB) and methylene blue (MB) were chosen as cationic molecules while methyl orange (MO) was selected as an example of anionic dye. The photocatalytic test device was equipped with an Osram Ultra-Vitalux lamp (300 W, $\lambda > 364$ nm) acting as artificial solar light source. Considering all device's parameters (the distance between the lamp and the surface of the solution, the power of the lamp and the dimensions of the used beaker) the irradiance was estimated at 600 $W.m^{-2}$.

In a typical test, photocatalytic powder (0.5 $mg.mL^{-1}$) was dispersed in pollutant solution at a concentration equal to 1.10^{-3} $mol.L^{-1}$. A vigorous stirring in the darkness during one hour was necessary to reach an equilibrium of the adsorption-desorption phenomenon between the particles and the pollutant molecules. Then, the solar light was switched-on and the mixture was irradiated. 3 mL of the suspension were collected at regular time periods during irradiation. After removal of the powder, the samples were analyzed by UV-visible spectrophotometry. The evolution of the pollutant concentration was estimated by colorimetric method considering the absorbance at 554, 664 and 464 nm for, respectively, RhB, MB and MO.

In parallel, for MB pollutant, the degradation advancement was investigated by qualitative and quantitative determination of the derivatives present in the suspension after different irradiation times, by LC-MS analysis. For this, 3 mL of the suspension were collected just before irradiation (*i.e.* after adsorption/desorption equilibrium was reached), and after 60, 120 and 180 min of irradiation. They were centrifuged to remove powder and stocked under nitrogen and obscurity at 4 °C until they could be injected in the chromatograph. All experiments for LC-MS analysis were performed in triplicate.

The formation of oxidative radicals in the photocatalytic process was investigated using scavenger coumponds: isopropanol (IPA), ethylenediamine tetraacetic acid disodium salt (EDTA) and benzoquinone (BQ) to trap •OH, h^+ and $\bullet O_2^-$, respectively.

3. Results

3.1. Characterization of photocatalysts

The as-prepared Au/WO_3 nanocomposite was firstly characterized by microscopic techniques. As a representative example of the distribution in gold nanoparticles (AuNPs) on the surface oxide catalyst, the SEM image of the WO_3 sample after Au deposition is given in Figure 1. It shows a rather dense collection of well distributed AuNPs on the basal facets of the support. The size distribution of gold nanoparticles, obtained by counting 1 000 particles, is given in inset. It shows a polydisperse size with a mean diameter of 7 ± 3 nm.

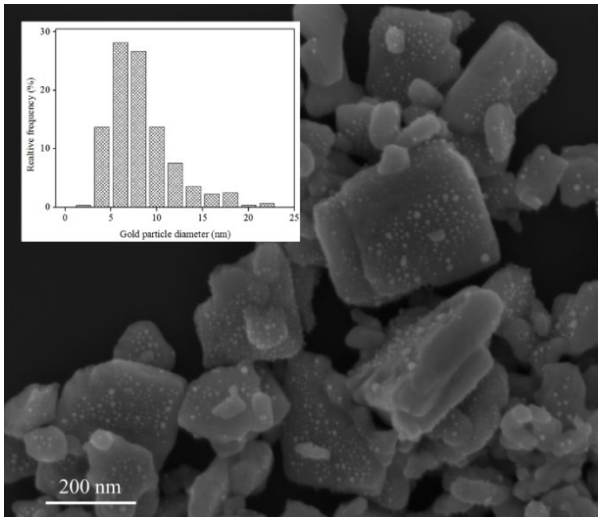

Figure 1: SEM image of Au/WO_3 nanocomposite. The inset represents the size distribution of gold particles performed on 1 000 particles.

TEM images, presented in Figure 2a and Figure 2b, show that AuNPs are essentially hemispherical thus optimizing the interfacial contact between the metal and the semiconductor. Interestingly, it is also observed that AuNPs preferentially decorate the basal flat facets of WO_3 nanoplatelets rather than lateral facets. On the Figure 2b, which shows a WO_3 platelet edge-on, no AuNP is observed on the lateral facet. Fast Fourier transforms (FFT) of the HR-TEM images were carried out (insert in Figures 2a and 2b), they showed that the platelets are a single crystal and all diffracted planes match with an orthorhombic phase, in agreement with XRD results presented in the next paragraph. Figure 2a corresponds to a platelet viewed along the

[010] direction so the (200) and the (002) planes are imaged. The platelet in Figure 2b is oriented with the b axis in the image plane, this particle orientation is such that only the (020) planes are imaged. Therefore, the basal facet of WO_3 platelets corresponds to (020) plane while the lateral facets may correspond to (200) or (002) planes. Hence, it is possible to conclude that AuNPs preferentially growth on (020) crystal planes of the WO_3 support. The Figure 2c shows defects that look like pores on the basal surface, it seems that the AuNP localized preferentially near theses defects. On the Figure 2d, which shown a platelet oriented along the [100] direction, defects on the pilling up of the (020) planes are observed (arrows). This type of defect leads to a streak of the spots along b* axis in the FFT (insert on the right of image 2d). On the FFT performed on reduced areas (inserts on the left of image 2d), no streaks are observed, the selected zones correspond to a part of crystal without defects.

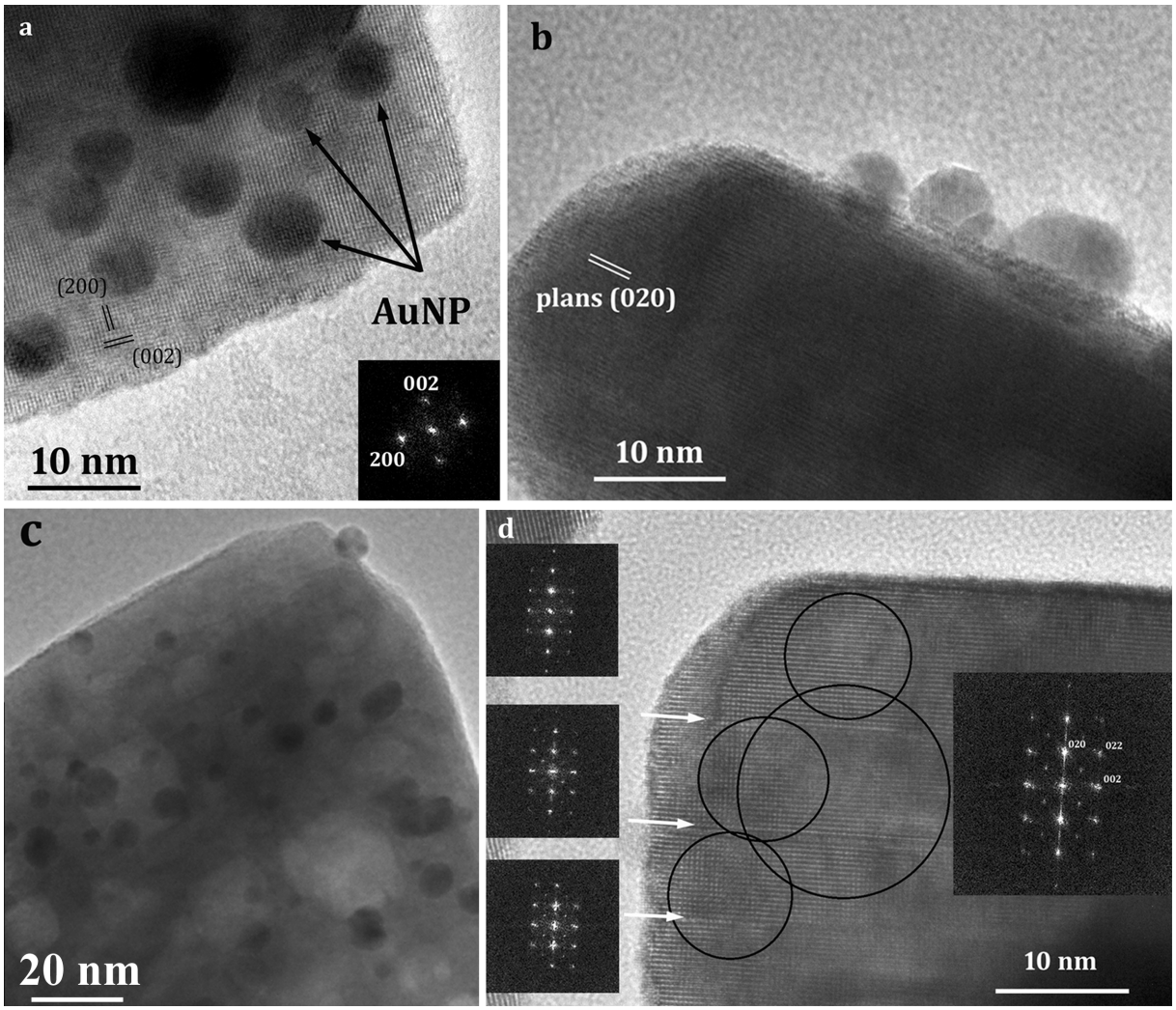

Figure 2: Images of gold nanoparticles deposited on WO_3 platelet:(a) platelet lying flat, the associated FFT corresponding to a [010] zone axis in insert; (b) platelet edge on with the (020) planes imaged; (c) defects like pores are observed on the (020) basal surface and (d) HREM of platelet oriented along the [100] direction, the circles corresponds to the selected areas of the FFT presented in inserts

The gold content was determined by ICP-AES. The results showed a concentration of 3.5 wt.% in gold for the composite sample while the assumed gold loading was 5 wt. %. This indicates a gold loading yield success of 70 % by the impregnation-reduction route.

XRD analysis were secondly performed to determinate the structure after gold deposition. Figure 3a shows the XRD pattern of WO_3 and Au/WO_3 samples. The patterns are very similar except the presence of three supplementary diffractions lines in the Au/WO_3 pattern. Those lines located at $2\theta = 38.27$, 44.60 and 64.68

degrees can be well indexed to, respectively, (111), (200) and (220) peaks of cubic gold structure (ICSD card no. 52249). All other diffraction peaks are common with the XRD pattern of bare WO_3 and can be well assigned to WO_3 orthorhombic structure (ICSD card no. 836) which was the platelet's crystalline structure before gold deposition, meaning that the used technique did not modify the bare support structure. Basically, WO_3 is crystallized in a deformed cubic structure, which can correspond either to a monoclinic phase or to an orthorhombic one. To settle between these two phases, electronic diffraction and Rietveld refinement were necessary and all the calculation details are available in our previous work (Desseigne et al., 2019).

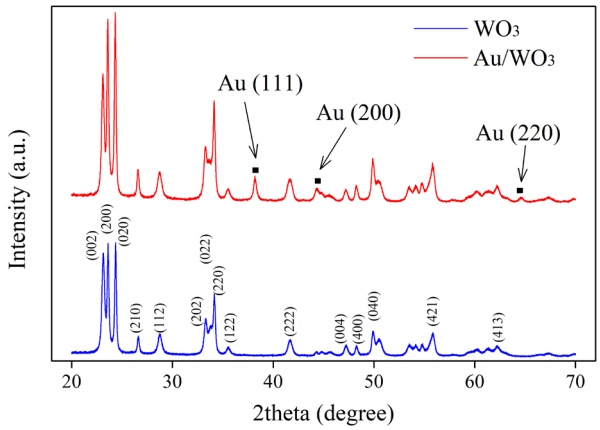

Figure 3: XRD patterns of bare WO_3 (blue) and Au/WO_3 nanocomposite (red)

As seen in Figure 4a, the XPS spectrum of Au/WO_3 sample showed the Au, W and O elements coexistence, as expected. The XPS spectrum of bare WO_3 showed residual sodium which can be attributed to impurities coming from the WO_3 platelet synthesis procedure. Figure 4b displays the 4f energy level for pure Au element with the $4f_{7/2}$ peak at 83.97 eV and the $4f_{5/2}$ peak at 87.64 eV. This confirms that gold is well reduced in its metallic state. Figure 4c depicts the binding energy of W $4f_{7/2}$ peak at 35.71 eV and W $4f_{5/2}$ peak at 37.84 eV, in accordance with the energy values found in the literature for W^{6+} cation (Katrib et al., 1995; Li et al., 2016; Shpak et al., 2007). This suggests that W is mainly in the (+VI) state in the Au/WO_3 nanocomposite. Figure 4d represents the 1s energy level of oxygen which was decomposed in three different peaks. The major peak is located at a maximum of 530 eV and corresponds to O^{2-} anions of the crystalline network, the peak located at 531 eV corresponds to $^{-}$OH hydroxyl groups (Dupin et al., 2000)

and the part of the peak at 533 eV is attributed to H_2O water molecules (Wagner et al., 1979). Moreover, the XPS analysis on the bare WO_3 powder permitted to confirm a ratio of 3 between the atomic concentrations of tungsten and oxygen (**see supplementary information**) which is in agreement with the expected stoichiometric coefficient.

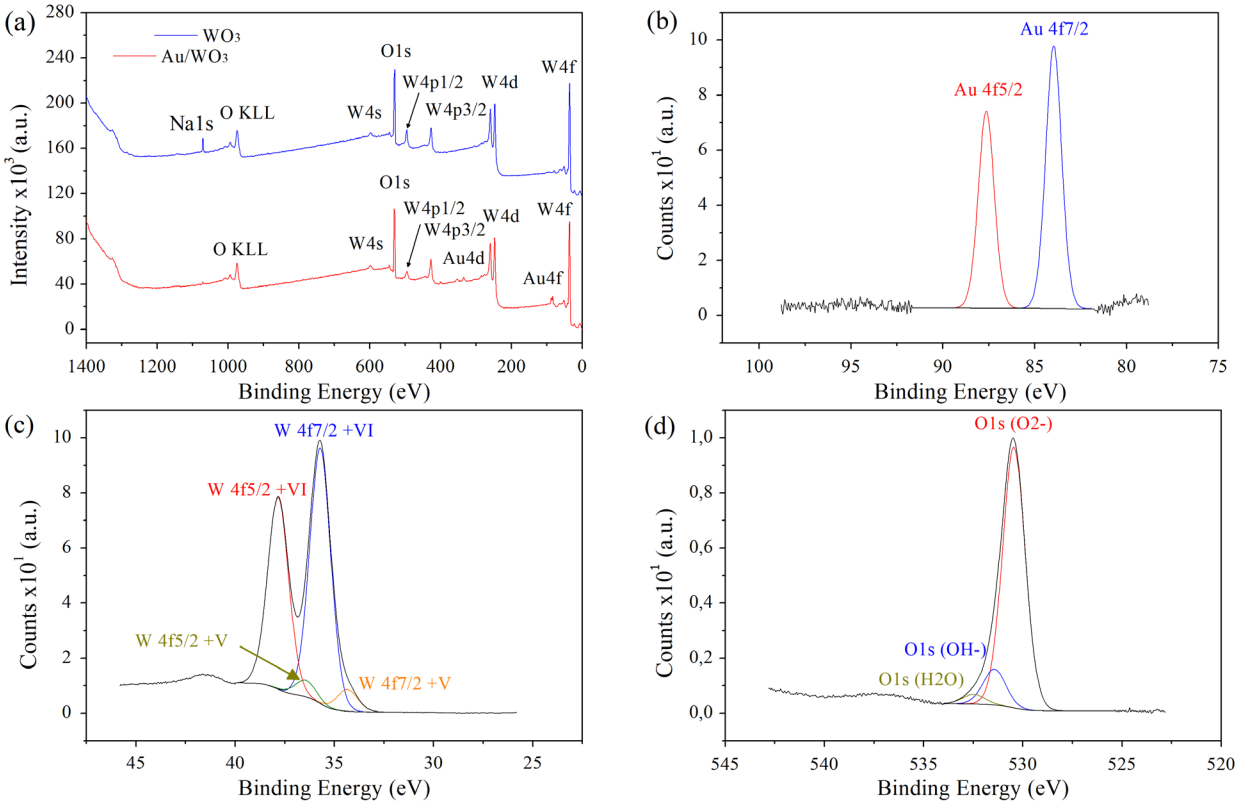

Figure 4: (a) XPS pattern of all elements for bare WO_3 and Au/WO_3; (b-d) High-resolution measurements on 4f levels of Au (b), W (c) and 1s level of O (d) for the Au/WO_3 composite.

The N_2 sorption isotherm of both WO_3 and Au/WO_3 samples are presented in Figure 5. The inspection of the high-pressure behavior (inset in Figure 5a) evidenced a hysteresis between the adsorption/desorption branches and a small plateau at the saturation pressure. Both isotherms can thus be assigned to type IV isotherm typical of a mesoporous system with relatively large pores considering the location of the sorption branches. The Barret-Joyner-Halenda (BJH) method (Barrett et al., 1951) was applied on the desorption branches and the obtained pore-size distribution is given in Figure 5b. The mean pore size around 60 nm for the bare WO_3 support is characteristic for an inter-granular porosity (between the platelets) and is

consistent with the SEM images presented in Figure 2. Addition of AuNPs leads to a strong decrease of the mean pore size that reaches 35 nm. This cannot solely be explained by the presence of the AuNPs whose size and concentration are too small to explain such variation. One hypothesis could be that the AuNPs incorporation procedure (impregnation, reduction and drying) on the WO_3 support modified the agglomeration state of the WO_3 platelets making them more compact, thus reducing the inter-granular porosity. The specific surface area was calculated using the Brunauer, Emmet and Teller (BET) equation. The obtained values are 12 $m^2.g^{-1}$ and 16 $m^2.g^{-1}$ for the bare WO_3 support and the Au/WO_3 composite, respectively. The increase of the BET area for the Au/WO_3 composite is directly correlated to the presence of the AuNPs. The total measured BET area a_{BET}^{Au/WO_3} can be directly written as in Equ. 1 where x_{Au} and x_{WO3} are, respectively, the weight fraction of WO_3 and Au in the composites. Furthermore, the platelet particles thickness was confirmed by applying the method of André *et al.* (André et al., 2012) by considering a density of 7.16 $cm^3.g^1$ and a side length of 166 nm (size determined by TEM) for our sample. The calculations lead to an average thickness around 31 nm which is in good agreement with SEM measures (23 ± 11 nm, **see supplementary information**).

$$\text{Equ. 1: } a_{BET}^{Au/WO_3} = x_{Au}\, a_{BET}^{Au} + x_{WO3}\, a_{BET}^{WO3}$$

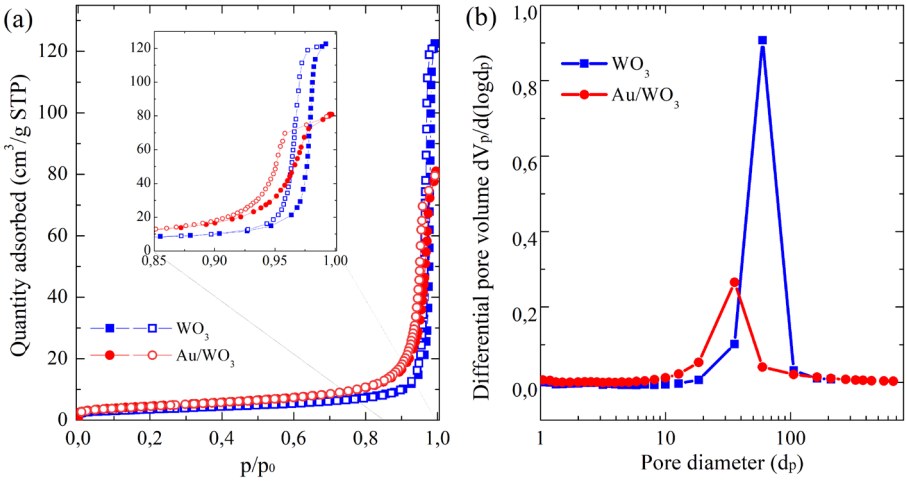

Figure 5: (a) N_2 sorption-desorption isotherms of bare WO_3 in blue and Au/WO_3 nanocomposite in red; (b) Distribution of the pore-size (BJH method)

The absorption spectrum of the Au/WO_3 sample (red curve) shown in Figure 6 exhibits two broad edge peaks. The first one centered on 300 nm is also observed in the absorption spectrum of pure WO_3 (Figure 6 blue curve) and corresponds to the optical band gap of the oxide support. The Kubelka-Munk plot in inset made possible the estimation of the band gap energy and the result lead to $E_g = 2.54$ eV. The second peak centered at around 550 nm corresponds to the surface plasmon resonance (SPR) band of gold nanoparticles (Hu et al., 2016). It is worth noting that the intensity of this peak is quite low compared to the main peak of WO_3. This is nevertheless consistent with literature where it has been demonstrated that the intensity of the absorbance peak of deposited AuNPs on oxide is strongly dependent on the particle size. Too small gold particles with diameter inferior to 5 nm could not have a SPR effect perceptible in diffuse reflectance spectra (Sarina et al., 2013), and in our case, the particles have an average size of 7 ± 3 nm which explains their low absorbance peak intensity.

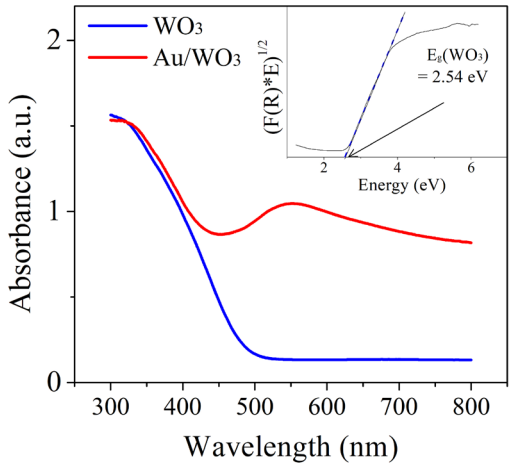

Figure 6: Absorbance spectra of bare WO_3 (blue curve) and Au/WO_3 composite (red curve). The inset corresponds to Kubelka-Munk plot used to determine the band gap energy

The photoresistance response (PRR) can be an effective method to examine the separation efficiency of photogenerated charges. As it can be seen in Figure 7a and Figure7b, the two samples (WO_3 and Au/WO_3) produced different photoresistance responses under an on-off cycle of photoirradiation at $\lambda > 364$ nm. First, the intrinsic resistance of the sample must be reached and stabilized, then the irradiation can be started which generates photoelectron-hole pairs and leads to a decrease of the resistance. A plateau was reached

when the photogenerated electron rate has stabilized and the irradiation was then switched off. The charge carriers' recombination occurred more or less quickly, depending on the photocatalyst electrical properties. As expected, the created Schottky barrier at the interface between gold nanoparticles and oxide semiconductor support exhibited the longest recombination period (25 time longer than bare WO_3) (Liu et al., 2020). For the nanocomposite sample, the enhancement of charge carriers' lifetime could be explained, on the one hand, by hot electrons which are produced when gold nanoparticles are irradiated due to its gold's SPR property. These hot electrons are transferred in the semiconductor's conduction band provided that their energy is higher than the band gap energy. In our case, we already proved by UV-visible spectroscopy and DRS measurements that our composite is photosensitive at wavelength located in the visible range thanks to $E_g(WO_3)$ = 2,54 eV. The hot electrons injections lead to an electrons overpopulation which allow a continuous electrons power supply. This results in a lower kinetic of the resistance to reach the equilibrium value hence a better charge carriers' lifetime. Figure 8 illustrates the hot electrons injection phenomenon. E_C, E_V and E_F are respectively the energy level of the conduction, valence and fermi band; $e\phi_m$ and $e\phi_{SC}$ are respectively the work function for the metal and for the semiconductor and VL means vacuum level (He et al., 2002; Hu et al., 2016; Sarina et al., 2013). On the other hand, under irradiation, the photons' electric field intensity at the surface of plasmonic nanoparticle is exacerbated which induce a localized SPR effect. This results in an important slowdown in the diffusion of photogenerated holes in the semiconductor which increase the return time at the equilibrium state of the charge carriers (Christopher et al., 2011; Link and El-Sayed, 2003).

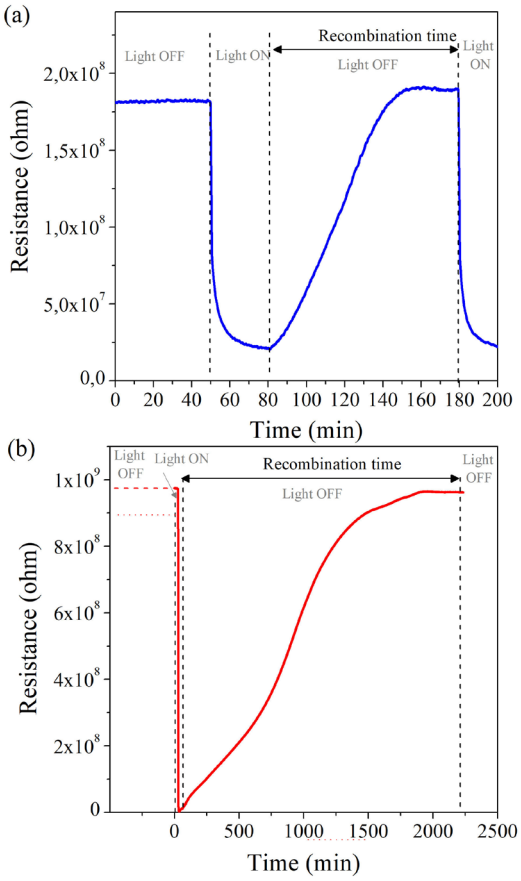

Figure 7: Photoresistance response after solar light irradiation of (a) WO_3 and (b) Au/WO_3 samples

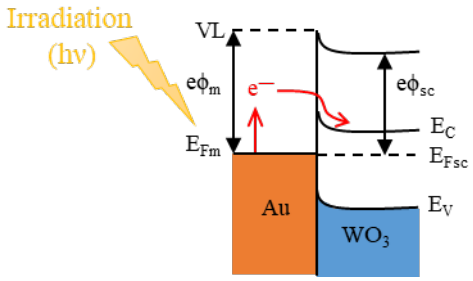

Figure 8: Schematic illustration of the hot electrons injection from irradiated plasmonic gold nanoparticles to WO_3 semiconductor.

3.2. Efficiency of photocatalytic activity

The photocatalytic activity of the Au/WO_3 nanocomposite was studied by the degradation under solar light irradiation of three model dyes like: rhodamine B (RhB), methylene blue (MB) and methyl orange (MO). The degradation efficiency depends on two main phenomena, the first one is the adsorption rate of the organic molecule onto the photocatalyst surface and the second one is due to the photoexcitation reaction occurring under irradiation.

3.2.1. Adsorption phenomenon

The adsorption rate was estimated by comparing the UV-visible spectra of the initial dye solution and the solution after reaching adsorption/desorption equilibrium. In general, the adsorption phenomenon depends on numerous factors such as the specific surface area, the steric hindrance related to organic molecules' interactions between adsorbent/adsorbate and the surface charge. As it can be seen in Figure 9, the bare oxide photocatalyst showed a selective adsorption depending on the charge and on the nature of the dye molecule. The zeta potential of the WO_3 powder dispersed in water was found to be – 41 mV [55] which indicates that the surface of the compound is highly negatively charged at natural pH. This creates suitable conditions for an electrostatic interaction with positively charged molecules. For MO, as expected for an anionic molecule, there was no adsorption for both bare WO_3 and Au/WO_3 nanocomposite. Interestingly, the adsorption behavior of WO_3 showed a huge difference between RhB and MB while both of them are cationic molecules; there is no adsorption for RhB whereas MB is adsorbed almost at 90 %. The strong attraction between MB and WO_3 might be favored by the high sulfur-oxygen affinity and the low steric hindrance around the cationic charge. On the contrary, the steric repulsion of the carboxylate anions in RhB might inhibits the extent of adsorption [56] on the WO_3 surface. The ca. 20 % decrease in MB adsorption rate in presence of the Au/WO_3 sample might be explained by the reduction of the porosity (change from 60 nm to 30 nm), due to the formation of gold nanoparticles which decrease adsorption site number.

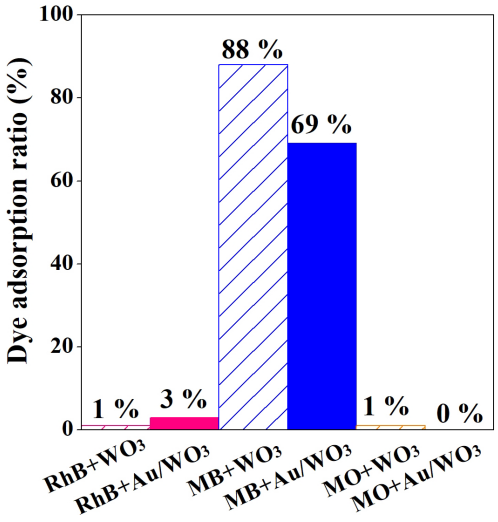

Figure 9: Dye adsorptipn ratio onto the photocatalyst's surface

3.2.2. Photocatalysis process

The photocatalytic efficiency results were determined from UV-visible spectra corresponding to different samples collected at periodic time during the irradiation time. Figure 10a, b and c show spectrum in the case of RhB, MB and MO respectively degraded by the nanocomposite. Previously to focus on the degradation induced by the photocatalysts, it is important to evaluate the self-degradation (*i.e.* photolysis) of each studied dye under solar light irradiation. These reference plots are shown by the black cross plot in Figure 10d, e and f for respectively RhB, MB and MO. Only MB is significantly sensitive to irradiation with a concentration loss of 30 % in 180 min. The photodegradation efficiencies are presented by empty square plot for pure WO_3 photocatalyst and full square plot for the gold decorated photocatalyst. The concentration at the initial irradiation point t_0 corresponds to the concentration after adsorption (C_0), in that respect, the concentration evolution (C_t) is only due to the photosensitive effect. RhB and MO dyes are only degraded in presence of the Au/WO_3 nanocomposite. The degradation under solar light irradiation reaches 100 % after 90 min for RhB and almost 50 % after 180 min for MO. Thus, a twice higher degradation rate can be reached in a twice shorter time for RhB than for MO. These differences might be associated with the charge of the molecules. The photocatalysis being a surface reaction, it might be expected that an attractive interaction will promote the photocatalytic efficiency while a repulsive interaction will hinder the

degradation process. The higher reactivity of Au/WO_3 photocatalyst with RhB pollutant is confirmed by the pseudo-first order plots presented in **supplementary information** from which the kinetic constant rate was calculated to be about 33.10^{-3} min 1 which is 3.3 times faster than for MB and 11 times faster than for MO. Although, MO has a lower degradation rate than the other two dyes, the efficiency of our nanocomposite photocatalyst towards the photodegradation of this specific dye noteworthy compared to some results in the literature where no degradation occurred with a similar Au/WO_3 material (Qamar et al., 2011). Due to a high adsorption of MB onto the pure WO_3 photocatalyst's surface before irradiation, a screening effect appeared which restricted the reactive oxygen species (ROS) production. As a result, the degradation started only after one hour of irradiation and reached 65 % after 180 min. In the case of gold decorated photocatalyst, the degradation started as soon as irradiation begins and no screening effect was observed leading to a better degradation rate which reached 81 % at the end of the test. From those observations, it can be concluded that AuNPs onto WO_3 nanoplatelets enhanced the efficiency of the photocatalyst whatever the dye's ionic charge.

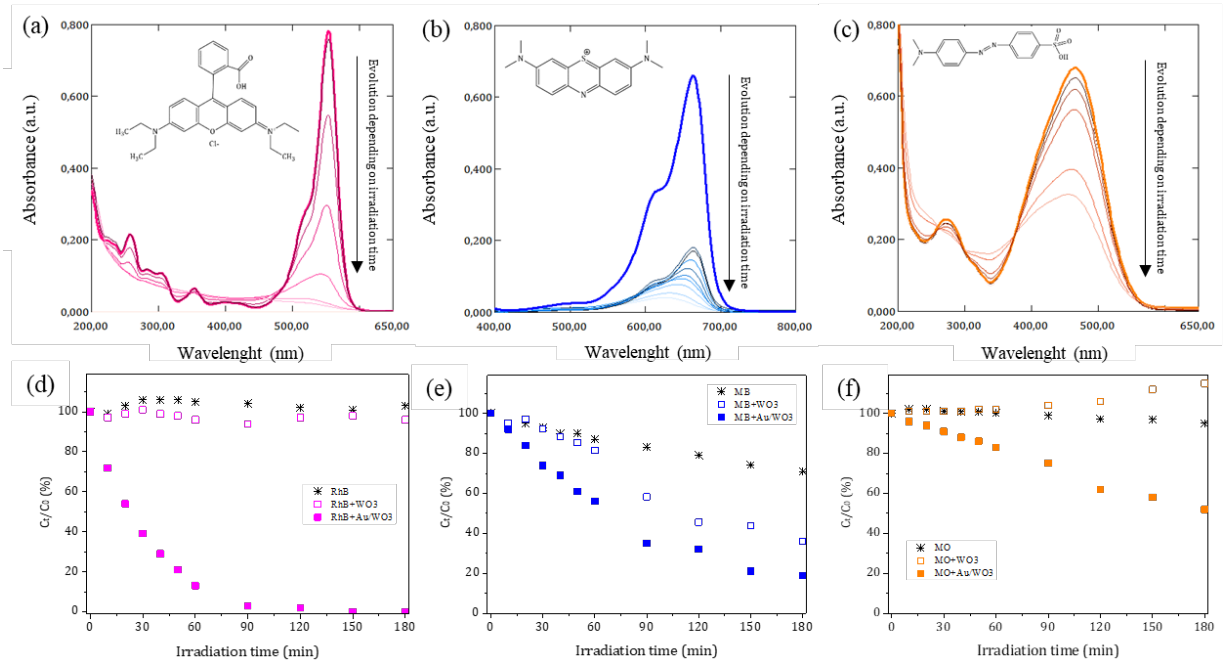

Figure 10: (a, b, c) Evolution of dye UV-vis. spectra during irradiation time with Au/WO_3 photocatalyst and (c, d, e) Evolution of relative dye concentration vs irradiation time for RhB (pink), MO (blue) and MO (orange). C_0 and C_t correspond to the initial dye concentration and the one at t time of irradiation, respectively.

Generally, the photodegradation mechanism starts when the semiconductor absorbs photons from the irradiation source generating pairs of electron – hole (Equ. 2). Then, three main species can lead to an efficient degradation in this system: (i) hydroxyl radicals •OH produced by WO_3 (Equ. 3 and 4), which are well known to have a high oxidative power at the conduction band level; (ii) superoxide radicals $\bullet O_2^-$ allowed by the presence of gold particles (Equ. 5 to 7) which can produce other ROS through reactions with water (Equ. 8 to 10) and, (iii) holes h^+ which react directly with the organic molecule at the catalyst surface. In addition, the photoexcited electrons within the photocatalyst might transform blue MB and pink RHB molecules into their colorless leuco form (LMB and LRhB respectively), as well as orange MO molecules into their colorless reduced form (MOH_2) , resulting in the photobleaching of their respective solution. With the Au/WO_3 photocatalyst, the conduction band energy level (E_{CB} = +0.82 V/NHE) only provide RhB to be directly reduced ($E_{RhB/LRhB}$ = +0.95 V/NHE, $E_{MB/LMB}$ = +0.53 V/NHE [58], $E_{MO/MOH2}$ = +0.24 V/NHE (pH=0) [59]). Yet for MB and MO, this reduction cannot straightly be ruled out because of the hot electrons generated in AuNPs by SPR effect. Nevertheless, there is evidence that potential MB photobleaching was followed by a real decomposition process like a gradual blueshift of the MB peak absorbance at 664 nm (Figure 10b) as expected in an oxidative demethylation of the dye molecule (Zang et al., 1995). Moreover, this demethylation will be demonstrated and confirmed hereafter with LC-MS analysis.

Equ. 2: $WO_3 + h\nu \longrightarrow h^+(WO_3) + e^-(WO_3)$

Equ. 3: $h^+(WO_3) + {}^-OH \longrightarrow \bullet OH$

Equ. 4: $h^+(WO_3) + H_2O \longrightarrow \bullet OH + H^+$

Equ. 5: $Au + h\nu \longrightarrow hot(e^-) + hot(h^+)$

Equ. 6: $4\ hot(h^+) + 2H_2O \longrightarrow O_2 + 4H^+$

Equ. 7: $O_2 + hot(e^-) \longrightarrow \bullet O_2^-$

Equ. 8: $\bullet O_2^- + H_2O \longrightarrow HO_2\bullet + {}^-OH$

Equ. 9: $HO_2\bullet + H_2O \longrightarrow H_2O_2 + \bullet OH$

Equ. 10: $H_2O_2 + h\nu \longrightarrow 2{\bullet}OH$

In order to better understand which reactive species played a role in the degradation pathway, trapping tests were performed and the results are presented in Figure 11. As a reminder, the scavenger solutions of IPA, EDTA and BQ made trapping tests possible for •OH, h^+ and $\bullet O_2^-$, respectively. The RhB photocatalytic efficiency was highly impacted with the presence of IPA contrary to EDTA and BQ which means that the degradation is mainly due to •OH. Only •OH trapping solution had an influence on the MB degradation while all scavengers impacted the efficiency of MO decomposition. Indeed, on the one hand, a degradation was observed when •OH and $\bullet O_2^-$ were trapped in MO solution which indicates that both oxygen radicals play a major role in the photoreaction mechanism; on the other hand, photogenerated h^+ seem to also play a role but minor than other species. In sum, the degradation with the Au/WO_3 nanocomposite under solar light irradiation is due to all created ROS for MO and only due to •OH for MB and RhB with a better degradation kinetic for RhB thanks to a direct oxidation with the photocatalyst.

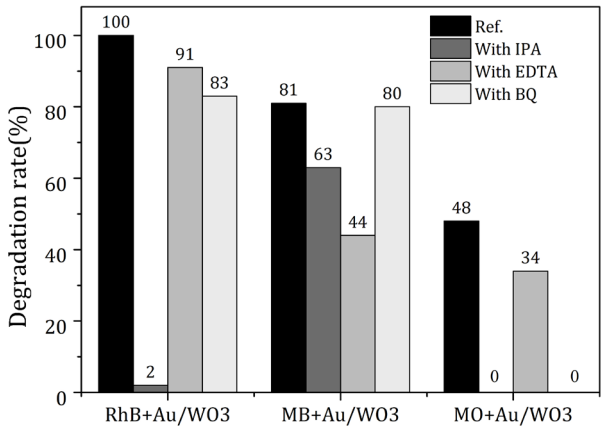

Figure 11: Results of trapping tests for nanocomposite with all dyes under solar light irradiation

Thanks to all results, the interactions between the solar light, nanocomposite photocatalyst and dye molecules can be summarized by the illustration in Figure 12.

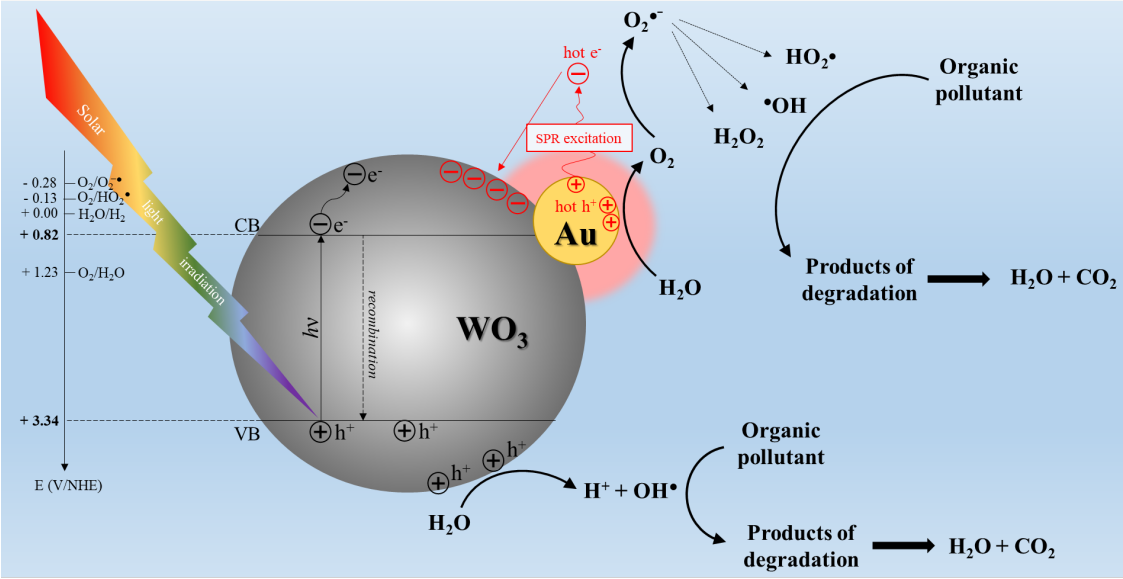

Figure 12: Illustration of dyes degradation mechanism in presence of Au/WO_3 under solar light irradiation

As MB is the only dye undergoing a degradation by photolysis, we performed further investigation in order to confirm the efficiency of our photocatalyst to really decompose it (thus eliminating the hypothesis of simple photobleaching) and to give an idea of the degradation pathway. In fact, in taking into account the valence band position of WO_3 (E_{VB} = +3.36 V/NHE), re-oxidation of the colorless reduced form of MB, the leuco methylene blue (LMB), by holes is highly thermodynamically favored. This would lead to a re-coloration of the solution and distort the estimated concentration. This kind of observation was already observed in the case of TiO_2 based photocatalysts exposed to aerated conditions (Lee et al., 2005) or visible light irradiation (Wang et al., 2014). In order to confirm a "real" degradation of MB by our photocatalyst, we performed liquid chromatography coupled with mass-spectrometry analyses. The concentration evolution throughout the irradiation was evaluated by the area of the chromatogram pic relevant to MB molecule (*i.e.* pic corresponding to mass and charge ratio m/z = 284). The relative concentration *vs* the irradiation time is presented in Figure 13 and compared with UV-visible spectroscopy results.

A huge difference between the concentration evolution of MB, during photolysis and photocatalysis with pure WO_3, respectively determined from UV-vis. spectra and LC-MS chromatograms appeared. Instead to have a continuous decrease as observed with UV-visible spectroscopy method, the observed degradation by chromatography method started after a plateau until 120 min and 60 min for photolysis and

photocatalysis, respectively. This highlights that the first degradation part of MB is not really a degradation but the formation of colorless LMB molecule. It also highlights the limit of UV-visible spectroscopy method and the importance to use a more sensitive technique to quantify the dye degradation yield. In contrast, similar results between the two analytical methods were obtained in presence of Au/WO_3 photocatalyst meaning gold decoration of the material is an efficient way to promote its activity under visible light and induce the decomposition of MB dye.

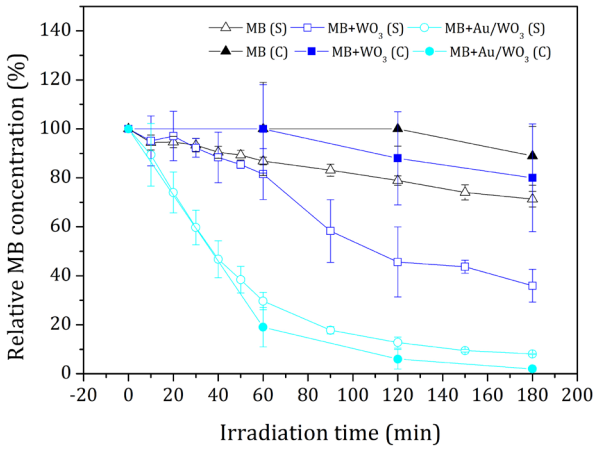

Figure 13: Evolution of relative concentration of MB during photolysis test (λ = 664 nm) determined from UV-visible spectra and LC-MS chromatographs (m/z = 284). S and C mean spectroscopy and chromatography method, respectively

3.2.3. Dyes degradation mechanism

Table 1 represents the detected fragments of molecule for the MB photolysis and MB photocatalysis occurred with WO_3 and Au/WO_3 after 60, 120 and 180 min of irradiation; The molecule formula of all m/z can be associated regarding the Figure 14 which represents the degradation pathway of MB according to LC-MS results. Two kind of reaction can initiate the MB decomposition. The first reaction is an oxidation of MB molecule (m/z = 284) by the •OH radical which can occurr either on the amine function to form an aldehyde (m/z = 298) or on the cycloalkanes (m/z = 300a) or on the heterocycle (m/z = 300b). The second reaction is a demethylation of the initial MB molecule (m/z = 270, 256, 242). The subsequent oxidation of these degradation products leads to a progressive mineralization until the ring opening (m/z = 193, 217, 229) and carbon chain fragmentation. Both the reactions ways occurred in competition for the three systems,

but only the Au/WO_3 nanocomposite material has the ability to oxidize the amine function of MB which seems to be the faster and more efficient way. The degradation by the demethylation is the slowest pathway because it needs to the creation of numerous intermediate fragments before the ring-opening. Due to the plasmonic properties of gold nanoparticles, the hydroxyl radicals are faster and greater created which explains the achievement of a decomposition until fragments with a ring-opening (m/z = 193, 217, 229) in only 180 min of irradiation. Because of the detection limit of the LC-MS device, it was not possible to observed lower fragments but, according to the literature, when the ring-opening is initiated for MB dye, then the mineralization is easy to reach. This conclude on the high efficiency of our nanocomposite photocatalyst for the MB degradation under solar light (Adachi et al., 2010; Cohen et al., 2019; DePuccio et al., 2015; Guo and Wang, 2019; Houas et al., 2001; Matsunami et al., 2019; Nguyen et al., 2019; Su et al., 2019; Wolski et al., 2019; Zhai et al., 2019).

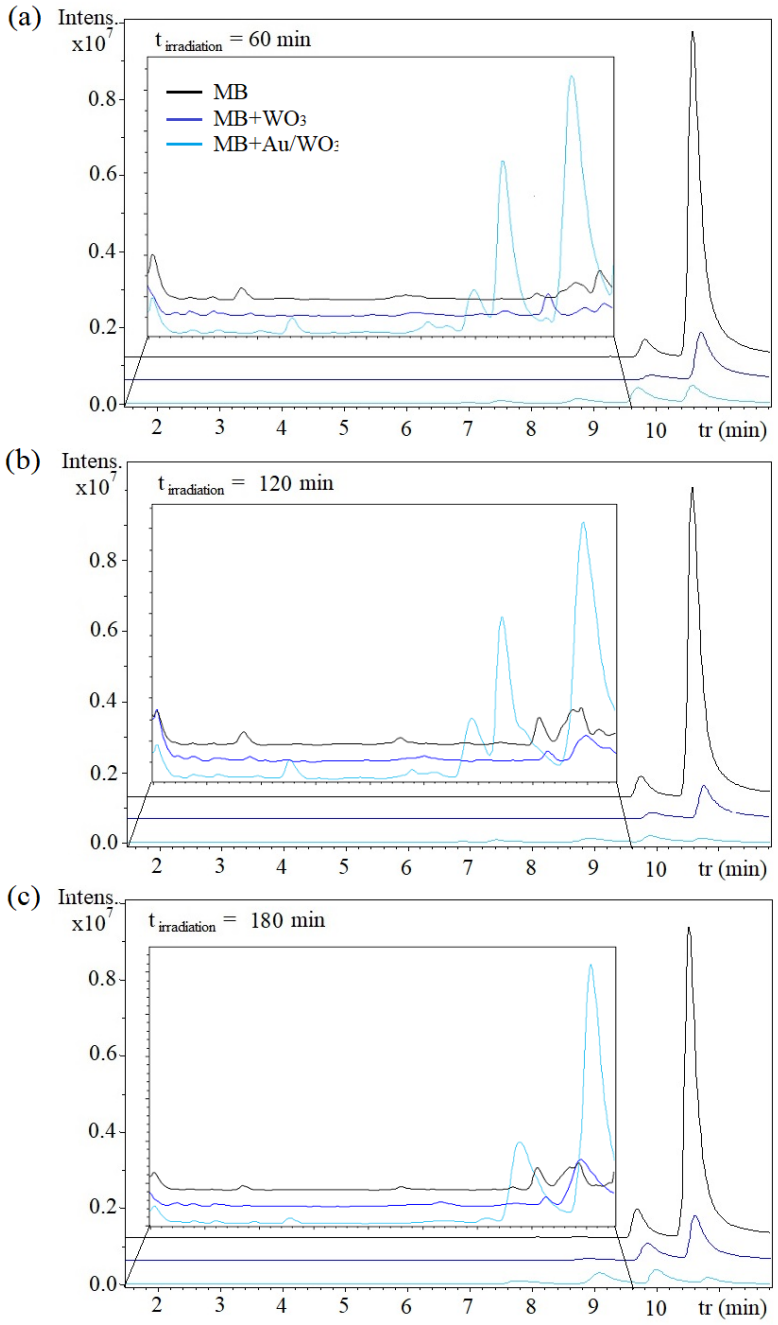

Figure 14: Chromatograms of MB degradation products obtained withou photocatalyst (black line), with bare WO_3 (dark blue line), and with Au/WO_3 photocatalyst (light blue line) at (a) 60, (b) 120 and (c) 180 min of irradiation

m/z	Retention time (min)	(a) MB			(b) MB + WO_3			(c) MB + Au/WO_3		
		Compound presents at a specific irradiation time								
		60	120	180	60	120	180	60	120	180
284	10.7	X	X	X	X	X	X	X	X	X
270[i]	9.9	X	X	X	X	X	X	X	X	X
256 [i]	8.9					X	X	X	X	X
261 [i]	1.8				X		X	X	X	X
305 [i]	2.4				X	X	X	X	X	X
393 [i]	4.5				X	X	X	X	X	X
229 [i]	8.3					X	X			
300 [ii]	6.7							X	X	
349 [ii]	2.8				X	X	X		X	X
217 [ii]	1.5				X	X	X	X		X
298 [iii]	7.6				X			X		X
314 [iii]	7.2							X	X	
193 [iii]	6.4								X	

Table 1 : Decomposition products detected by LC-MS analysis after 60, 120 and 180 min of irradiation by (a) photolysis and photocatalysis asssisted by (b) bare WO_3 and (c) Au/WO_3 nanocomposite. [i, ii, iii] means products from one of the three degradation pathway illustrated in Figure 15

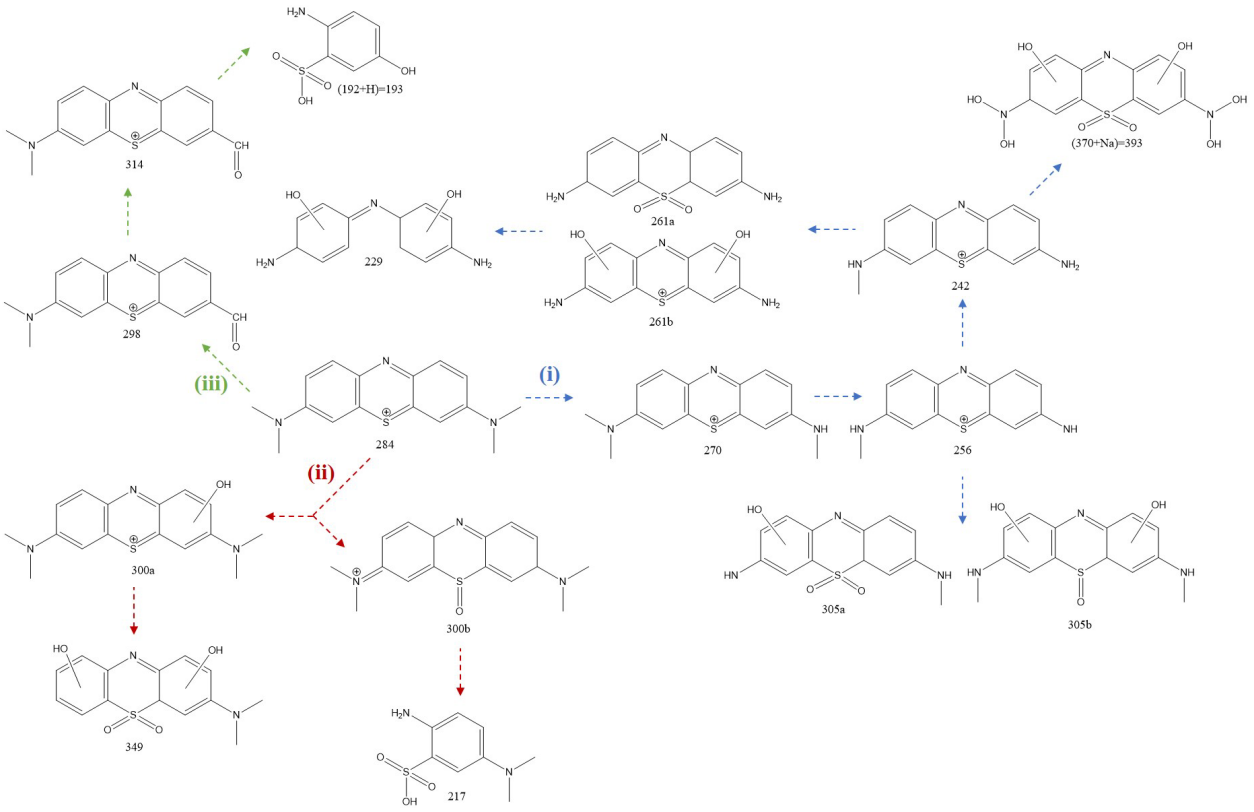

Figure 15: A proposition of the possible MB decomposition pathway by solar photocatalysis assisted by bare or gold decorated WO_3 nanoplatelets

4. CONCLUSION

We have prepared a nanostructured photocatalyst composed of WO_3 platelet-like support decorated with well distributed gold nanoparticles by a simple impregnation-reduction method. A deep TEM analysis revealed a preferential deposition of the gold nanoparticles on the basal facets (020) of platelets with a mean diameter of 7 nm. The single-step and room temperature gold decoration process used in this work did not induce any structural nor microstructural nor band-gap modification of characterization of the oxide support, but significantly affected its porosity and specific surface and strongly enhanced the charge carriers' lifetime (by a factor 25). The photocatalytic efficiency was performed on three aqueous model pollutants with different surface charges in presence of the bare WO_3 and the Au/WO_3 nanocomposite photocatalysts, for comparison. For all pollutants, Au/WO_3 photocatalyst showed a higher efficiency due to the plasmonic property and the interface creation between gold nanoparticles and WO_3 semiconductor

which highly improved electrical properties. This improvement was mainly highlighted by performing photoresistance measurement under solar light. Besides, the scavenger tests revealed that the •OH photogenerated radicals are the major oxidizing species for a cationic molecule (like RhB), while for an anionic molecule (like MO) both •OH and $•O_2^-$ radicals played a role in the degradation. For MB, a highly adsorbed dye onto the WO_3 platelets, LC-MS analyses were performed and results revealed an advanced oxidative process. It also showed that gold nanoparticles coupled with WO_3 permit to avoid any photobleaching reaction and led to a truly decomposition until ring opening and mineralization. Moreover, LC-MS investigations permitted to propose a MB degradation pathway in presence of Au/WO_3 photocatalyst under solar light irradiation.

5. ACKNOWLEDGMENTS

The authors gratefully acknowledge the Regional Council of Provence-Alpes-Côte d'Azur, General Council of Var, the urban community of Toulon Provence Mediterranean and University of Toulon for their financial support in the framework of the "NanoCat" project. The authors also wish to thank Professor Gerald CULIOLI and Bruno VIGUIER for allowing us to perform LC-MS analysis and for scientific discussions and advice.

6. REFERENCES

Adachi, K., Mita, T., Yamate, T., Yamazaki, S., Takechi, H., Watarai, H., 2010. Controllable Adsorption and Ideal H-Aggregation Behaviors of Phenothiazine Dyes on the Tungsten Oxide Nanocolloid Surface. Langmuir 26, 117–125. https://doi.org/10.1021/la902174s

André, B., Dumont, M., Rogez, J., Heresanu, V., Rufino, B., Bouchet, R., Denoyel, R., 2012. Morphology and reactivity of aluminium nanocrystalline powders. Int. J. Nanotechnol. 9, 618. https://doi.org/10.1504/IJNT.2012.045332

Barrett, E.P., Joyner, L.G., Halenda, P.P., 1951. The Determination of Pore Volume and Area Distributions in Porous Substances. I. Computations from Nitrogen Isotherms. J. Am. Chem. Soc. 73, 373–380. https://doi.org/10.1021/ja01145a126

Christopher, P., Xin, H., Linic, S., 2011. Visible-light-enhanced catalytic oxidation reactions on plasmonic silver nanostructures. Nat. Chem. 3, 467–472. https://doi.org/10.1038/nchem.1032

Cohen, M., Ferroudj, N., Combes, A., Pichon, V., Abramson, S., 2019. Tracking the degradation pathway of three model aqueous pollutants in a heterogeneous Fenton process. J. Environ. Chem. Eng. 7, 102987. https://doi.org/10.1016/j.jece.2019.102987

DePuccio, D.P., Botella, P., O'Rourke, B., Landry, C.C., 2015. Degradation of Methylene Blue Using Porous WO3, SiO2–WO3, and Their Au-Loaded Analogs: Adsorption and Photocatalytic Studies. ACS Appl. Mater. Interfaces 7, 1987–1996. https://doi.org/10.1021/am507806a

Desseigne, M., Dirany, N., Chevallier, V., Arab, M., 2019. Shape dependence of photosensitive properties of WO3 oxide for photocatalysis under solar light irradiation. Appl. Surf. Sci. 483, 313–323. https://doi.org/10.1016/j.apsusc.2019.03.269

Dirany, N., Arab, M., Madigou, V., Leroux, Ch., Gavarri, J.R., 2016a. A facile one step route to synthesize WO $_3$ nanoplatelets for CO oxidation and photodegradation of RhB: microstructural, optical and electrical studies. RSC Adv. 6, 69615–69626. https://doi.org/10.1039/C6RA13500E

Dupin, J.-C., Gonbeau, D., Vinatier, P., Levasseur, A., 2000. Systematic XPS studies of metal oxides , hydroxides and peroxides. Phys. Chem. Chem. Phys. 2, 1319–1324. https://doi.org/10.1039/A908800H

Guo, X., Wang, D., 2019. Photo-Fenton degradation of methylene blue by synergistic action of oxalic acid and hydrogen peroxide with NiFe2O4 hollow nanospheres catalyst. J. Environ. Chem. Eng. 7, 102814. https://doi.org/10.1016/j.jece.2018.102814

He, T., Ma, Y., Cao, Y., Yang, W., Yao, J., 2002. Improved photochromism of WO3 thin films by addition of Au nanoparticles. Phys. Chem. Chem. Phys. 4, 1637–1639. https://doi.org/10.1039/b108531j

Houas, A., Lachheb, H., Ksibi, M., Elaloui, E., Guillard, C., Herrmann, J.-M., 2001. Photocatalytic degradation pathway of methylene blue in water. Appl. Catal. B Environ. 31, 145–157. https://doi.org/10.1016/S0926-3373(00)00276-9

Hu, D., Diao, P., Xu, D., Wu, Q., 2016. Gold/WO3 nanocomposite photoanodes for plasmonic solar water splitting. Nano Res. 9, 1735–1751. https://doi.org/10.1007/s12274-016-1067-0

Katrib, A., Hemming, F., Wehrer, P., Hilaire, L., Maire, G., 1995. The multi-surface structure and catalytic properties of partially reduced WO3, WO2 and WC + O2 or W + O2 as characterized by XPS. J. Electron Spectrosc. Relat. Phenom., Proceedings of the Sixth International Conference on Electron Spectroscopy 76, 195–200. https://doi.org/10.1016/0368-2048(95)02451-4

Lee, S.-K., Sheridan, M., Mills, A., 2005. Novel UV-Activated Colorimetric Oxygen Indicator. Chem. Mater. 17, 2744–2751. https://doi.org/10.1021/cm0403863

Li, X., Lunkenbein, T., Kröhnert, J., Pfeifer, V., Girgsdies, F., Rosowski, F., Schlögl, R., Trunschke, A., 2016. Hydrothermal synthesis of bi-functional nanostructured manganese tungstate catalysts for selective oxidation. Faraday Discuss. 188, 99–113. https://doi.org/10.1039/C5FD00191A

Link, S., El-Sayed, M.A., 2003. Optical Properties and Ultrafast Dynamics of Metallic Nanocrystals. Annu. Rev. Phys. Chem. 54, 331–366. https://doi.org/10.1146/annurev.physchem.54.011002.103759

Liu, J., Xu, S.-M., Li, Y., Zhang, R., Shao, M., 2020. Facet engineering of WO3 arrays toward highly efficient and stable photoelectrochemical hydrogen generation from natural seawater. Appl. Catal. B Environ. 264, 118540. https://doi.org/10.1016/j.apcatb.2019.118540

Matsunami, D., Yamanaka, K., Mizoguchi, T., Kojima, K., 2019. Comparison of photodegradation of methylene blue using various TiO2 films and WO3 powders under ultraviolet and visible-light irradiation. J. Photochem. Photobiol. Chem. 369, 106–114. https://doi.org/10.1016/j.jphotochem.2018.10.020

Nguyen, T.B., Doong, R., Huang, C.P., Chen, C.-W., Dong, C.-D., 2019. Activation of persulfate by CoO nanoparticles loaded on 3D mesoporous carbon nitride (CoO@meso-CN) for the degradation of methylene blue (MB). Sci. Total Environ. 675, 531–541. https://doi.org/10.1016/j.scitotenv.2019.04.230

Qamar, M., Yamani, Z.H., Gondal, M.A., Alhooshani, K., 2011. Synthesis and comparative photocatalytic activity of Pt/WO3 and Au/WO3 nanocomposites under sunlight-type excitation. Solid State Sci. 13, 1748–1754. https://doi.org/10.1016/j.solidstatesciences.2011.07.002

Sarina, S., Waclawik, E.R., Zhu, H., 2013. Photocatalysis on supported gold and silver nanoparticles under ultraviolet and visible light irradiation. Green Chem. 15, 1814. https://doi.org/10.1039/c3gc40450a

Shpak, A.P., Korduban, A.M., Medvedskij, M.M., Kandyba, V.O., 2007. XPS studies of active elements surface of gas sensors based on WO3−x nanoparticles. J. Electron Spectrosc. Relat. Phenom., Electronic Spectroscopy and Structure: ICESS-10 156–158, 172–175. https://doi.org/10.1016/j.elspec.2006.12.059

Su, S., Liu, Y., Liu, X., Jin, W., Zhao, Y., 2019. Transformation pathway and degradation mechanism of methylene blue through β-FeOOH@GO catalyzed photo-Fenton-like system. Chemosphere 218, 83–92. https://doi.org/10.1016/j.chemosphere.2018.11.098

Wagner, C.D., Riggs, W.M., Davis, L.E., Moulder, J.F., Muilenberg, G.E., 1979. Handbook of X-ray Photoelectron Spectroscopy, Perkin-Elmer Corp. Eden Prairie MN 38.

Wang, W., Ye, M., He, L., Yin, Y., 2014. Nanocrystalline TiO_2 -Catalyzed Photoreversible Color Switching. Nano Lett. 14, 1681–1686. https://doi.org/10.1021/nl500378k

Wolski, L., Walkowiak, A., Ziolek, M., 2019. Formation of reactive oxygen species upon interaction of Au/ZnO with H2O2 and their activity in methylene blue degradation. Catal. Today, SI: 8WCOC 333, 54–62. https://doi.org/10.1016/j.cattod.2018.04.004

Zang, L., Liu, C.-Y., Ren, X.-M., 1995. Photochemistry of semiconductor particles 3. Effects of surface charge on reduction rate of methyl orange photosensitized by ZnS sols. J. Photochem. Photobiol. Chem. 85, 239–245. https://doi.org/10.1016/1010-6030(94)03918-K

Zhai, S., Li, M., Wang, D., Zhang, L., Yang, Y., Fu, S., 2019. In situ loading metal oxide particles on bio-chars: Reusable materials for efficient removal of methylene blue from wastewater. J. Clean. Prod. 220, 460–474. https://doi.org/10.1016/j.jclepro.2019.02.152